PAPER

Two-dimensional Cu(I)-MOF with mesoporous architecture towards chemiresistive NO$_2$ sensing†

Dilip Pandey,[a] Trivedi Samarth,[a] Vikash Kumar Verma,[b] Chandrabhan Patel,[b] L. Ponvijayakanthan,[c] Neeraj K. Jaiswal,*[c] Shaibal Mukherjee [ID] *[bde] and Abhinav Raghuvanshi [ID] *[a]

Conducting metal–organic frameworks (c-MOFs) have emerged as a promising platform for chemiresistive gas sensors due to their intrinsic porosity and ability to facilitate charge transfer upon gas adsorption. In this study, we report a semiconducting copper(I)-MOF (**Cu-MOF**) formed by the self-assembly of CuI and *N*-phenyl-*N*-(pyridin-4-yl)pyridin-4-amine. The **Cu-MOF** consists of a 2D network comprising Cu$_4$I$_4$ secondary building units, which forms an intercalating 3D structure driven by multiple weak interactions. The semiconducting nature and mesoporous structure motivated the exploration of its chemiresistive gas sensing capabilities. The chemiresistive device fabricated with **Cu-MOF** displays high selectivity and efficient room temperature NO$_2$ sensing with a lower limit of detection (3.5 ppb) and a swift response/recovery time (~11/13 s), one of the fastest among the reported state-of-the-art MOF-based NO$_2$ sensors. Experimental and theoretical analysis reveals that the adsorption of NO$_2$ on **Cu-MOF** withdraws electrons from the Cu(I) center, leading to a change in electrical response. The rapid response/recovery without any external stimuli, repeatability and material robustness further enhance its potential applications.

Introduction

Metal–organic frameworks (MOFs) have gained significant interest due to their porosity along with chemical and structural diversity, leading to multifunctional properties. Although the majority of MOFs are electrical insulators, the past decade has witnessed the emergence of several electrically conductive MOFs (c-MOFs).[1–3] c-MOFs are usually composed of π-conjugated ligands capable of effective charge delocalization and are highly attractive for various electronic applications, including electrocatalysis, sensing, energy storage, and quantum information.[4–10] In particular, 2D c-MOFs have emerged as promising candidates for the development of chemiresistive sensors.[11] Their porous structures and electrical properties improve gas adsorption and interactions while maintaining high electrical conductivity under ambient conditions.[4,7,10,12–15] Moreover, the presence of diverse binding sites in these materials enables unique interactions with specific target molecules, significantly enhancing selectivity. Therefore, the incorporation of c-MOFs has significantly addressed the key limitations associated with the selectivity and room temperature operation of traditional sensing materials for some toxic gases.[16–20] Recently, semiconducting Cu(I) frameworks have attracted considerable attention in the field of chemiresistive gas sensing due to their potential for detecting a wide range of volatile organic compounds and inorganic toxic gases such as NH$_3$, MeOH, NO$_2$, and others.[21–24] The tendency of CuI salts to assemble into different high-nuclearity clusters, such as [Cu$_2$I$_2$], [Cu$_3$I$_3$], [Cu$_4$I$_4$], *etc.*, and their structural diversity lead to attractive platforms for various applications.[25–29] These clusters contribute to the formation of semiconducting, tunable and robust frameworks, enhancing their potential for sensing applications. Furthermore, cost-effectiveness, low toxicity, and convenient synthesis make these materials even more attractive.

A significant discharge of industrial waste gases and automobile exhaust has caused considerable damage to the environment and human health. NO$_2$ is one of the commonly emitted toxic gases, contributing to ground-level ozone formation, acid rain, eutrophication, reduced visibility and climate change.[17,30] Low-level NO$_2$ exposure to humans can cause respiratory and cardiovascular issues, including bronchitis, pulmonary edema, and olfactory paralysis, whereas prolonged

[a]Department of Chemistry, Indian Institute of Technology Indore, Madhya Pradesh 453552, India

[b]Hybrid Nanodevice Research Group (HNRG), Department of Electrical Engineering, Indian Institute of Technology Indore, Madhya Pradesh 453552, India

[c]2-D Materials Research Laboratory, Discipline of Physics, PDPM Indian Institute of Information Technology Design and Manufacturing, Jabalpur, Madhya Pradesh 482005, India

[d]Centre for Advanced Electronics (CAE), Indian Institute of Technology Indore, Madhya Pradesh 453552, India

[e]School of Engineering, RMIT University, Melbourne, VIC 3001, Australia. E-mail: neeraj@iiitdmj.ac.in; shaibal@iiti.ac.in; r.abhinav@iiti.ac.in

† Electronic supplementary information (ESI) available. CCDC 2385865. For ESI and crystallographic data in CIF or other electronic format see DOI: https://doi.org/10.1039/d4ta07702d

exposure may lead to severe brain disorders such as Parkinson's disease, which can be life-threatening.[31–34] Toxicity by NO_2 arises due to its reaction with hemoglobin to form methemoglobin, which is unable to carry oxygen.[35] Therefore, quick and real-time detection of NO_2 is essential for public health and environmental monitoring. Several materials have shown promising results for room temperature NO_2 sensing, but response time and reversibility are still a major challenge. The irreversibility is attributed to NO_2's strong tendency to extract electrons from metal nodes and form stable complexes.[36,37] Strategies such as photoactivation and high-temperature operation have been employed to address this issue, leading to additional power requirements in the device. The success of these approaches cannot be undermined, but for real-world applications, sensors that can operate at room temperature without the requirement of any external stimuli would be more appropriate.[31,38] Recently, some copper(II) MOFs have been reported for NO_2 gas sensing; however, most of these materials either exhibit relatively long response times or require external stimuli for efficient sensing performance.[39,40]

In this study, we report a 2D copper(I)-MOF (**Cu-MOF**), synthesized from N-phenyl-N-(pyridin-4-yl)pyridin-4-amine (PDPA) and CuI. The **Cu-MOF** consists of a Cu_4I_4 secondary building unit (SBU). The semiconducting behaviour and mesoporous structure intrigued us to explore its gas-sensing capabilities. The chemiresistive gas sensor fabricated from **Cu-MOF** demonstrated a high selectivity and response for NO_2 gas with an exceptionally fast response/recovery time of approximately 11/13 seconds at room temperature. The sensing mechanism is thoroughly investigated using experimental and theoretical studies.
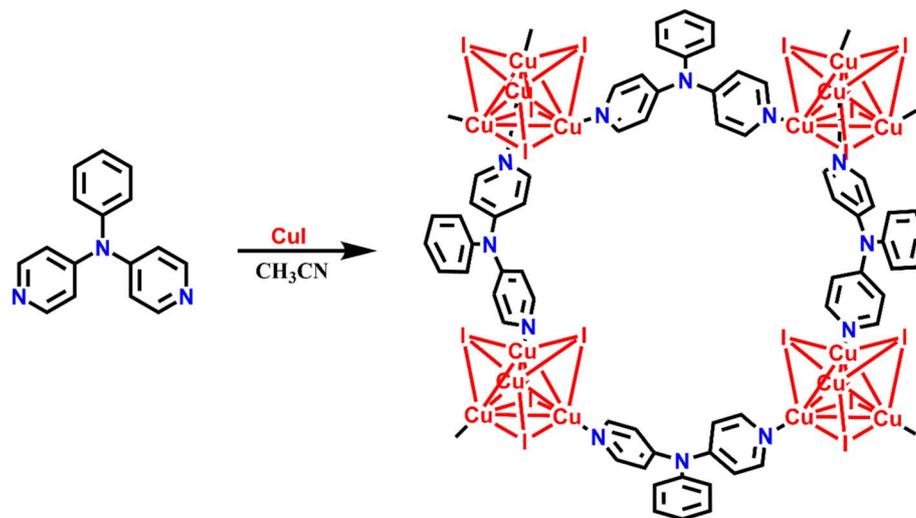
Results and discussion

The ligand, PDPA, was synthesized in 70% yield by reacting 4,4′-dipyridylamine with bromobenzene (Scheme S1†) and characterized with various spectroscopic techniques (Fig. S1–S4†). The synthesized ligand was reacted with CuI in a 1 : 2 ratio to obtain **Cu-MOF** as a white solid in 80% yield (Scheme 1). The synthesized MOF was initially analyzed using infrared spectroscopy, which showed slight shifts from the ligand spectrum, substantiating the coordination of the ligands with CuI (Figure S5†).

Crystals suitable for single-crystal X-ray diffraction (SCXRD) were obtained by slow diffusion of acetonitrile solution of CuI into a dichloromethane solution of the ligand over a week. **Cu-MOF** crystallizes in the monoclinic system with the Cc space group. Other important crystallographic parameters are given in Table S1.† The asymmetric unit consists of four copper, four iodides, and two ligand units (Fig. S6a†). The expanded structure reveals a two-dimensional network with Cu_4I_4 distorted cubane tetrameric SBUs. Each copper has distorted tetrahedral geometry and is bridged with μ^3-I and pyridyl nitrogens of the ligand. Both pyridyl rings of the ligand are coordinated to two different Cu_4I_4 clusters. These Cu_4I_4 SBUs are connected to adjacent Cu_4I_4 via the bridging of ligands, leading to a 2D framework with 44-membered metallacycles forming rectangular voids (Fig. 1a and

b). The distances between the centroid of adjacent clusters are 13.356 Å along vertical and 13.214 Å along horizontal axes (Fig. S6b†). In the Cu_4I_4 distorted cubane tetramer, Cu–I, Cu–N, and Cu–Cu distances are in the range of 2.624–2.748 Å, 2.023–2.047 Å and 2.624–2.698 Å, respectively (Fig. S7†). The angle of Cu–I–Cu is around 59°. These bond metrics are consistent with previous reports on Cu(I) iodide frameworks having Cu_4I_4 SBUs.[29,41–43] C–H–π interactions (2.805–2.898 Å) involving ortho and meta hydrogen of the phenyl ring lead to another entangled plane which is chemically equivalent to the 2D framework (Fig. 1d), partially filling the voids generated by the rhombus-grid structure. In addition, some solvent molecules are also found trapped in the cavity. Thus entangled planes and solvent molecules in the voids generated by the 2D network led to close packing in the crystal structure. Both sheets are nearly perpendicular to each other with a sliding angle of 77.75° (Fig. 1d). Such crystal structures packing in CuI clusters are previously reported with some other ligands.[43–46] Moreover, weak C–H···I (3.133 Å) interactions were also identified from para-hydrogen of the phenyl ring to iodine, leading to parallel stacking of sheets with interplanar distances of 12.776 Å (Fig. 1c). Thus, infinitely parallel 2D stacked sheets and 77.75° tilted 2D sheets form an intercalated close-packed 2D–3D mixed network.

The experimental powder X-ray diffraction (PXRD) patterns confirmed the phase purity of the bulk sample, which correlates well with the simulated pattern obtained from SCXRD analysis (Fig. S8a†). **Cu-MOF** remains stable for several months under ambient conditions. The thermal stability of **Cu-MOF** was assessed using thermogravimetric analysis (TGA) (Fig. S8b†), which suggests thermal stability until 250 °C. The Brunauer–Emmett–Teller (BET) analysis showed a type IV isotherm with a surface area of 15.033 m^2 g^{-1}, indicating a mesoporous structure for **Cu-MOF** (Fig. S9a†). Additionally, the pore size of **Cu-MOF** was determined to be 5.77 nm using the Barrett–Joyner–Halenda (BJH) method (Fig. S9b†). The surface morphology of the synthesized MOF was assessed using field emission scanning electron microscopy (FE-SEM). FE-SEM images suggest the formation of irregular agglomerated petals (Fig. 2). These multiple petals pile up to form nanoflower structures of different sizes. The petals have curved ending sides while they seem to have grown over each other (Fig. 2a–c). Energy dispersive X-ray (EDX) analysis confirms the uniform presence of Cu, C, N, and I elements in an appropriate portion in MOF (Fig. S10†). Moreover, elemental mapping analysis verified the uniform distribution of elements over the surface, demonstrating a consistent composition (Fig. 2d–g). Transmission electron microscopy (TEM) images also suggest the formation of agglomerated nano-particles of sizes ranging from 100 to 800 nm, with shades of darker color in a single particle, which could show the extent of accumulation (Fig. 2h and i). The selected area electron diffraction (SAED) pattern indicates rings corresponding to different diffraction planes present in **Cu-MOF**, pointing to the crystalline nature of **Cu-MOF** (Fig. 2j).

The optical band gap of **Cu-MOF** was measured from ultraviolet-visible diffuse reflectance spectroscopy (UV-Vis DRS) using the Tauc plot function (Fig. S11†). A band gap (E_g) of 2.04 eV was determined, suggesting the semiconducting nature of

This journal is © The Royal Society of Chemistry 2025

J. Mater. Chem. A, 2025, **13**, 11416–11424 | **11417**

Scheme 1 Synthesis of **Cu-MOF**.

Cu-MOF. Furthermore, the electrical conductivity of the pressed pellet of **Cu-MOF** was measured using a Keithley 6517B electrometer across a voltage range of −10 V to +10 V. The electrical conductivity was found to be 3.3×10^{-7} S cm^{-1}, confirming the semiconductor characteristics of **Cu-MOF** (Fig. S12†).

Gas sensing measurements

The 2D structure with accessible voids, favorable nanostructure morphology with the mesoporous nature of the material, and semiconducting behavior of **Cu-MOF** prompted us to explore its chemiresistive gas sensing behavior. **Cu-MOF** was mixed in ethanol, drop-cast onto interdigitated electrodes (IDEs, 1.5×1 cm), and then dried in the oven for 12 h. This sensing device was kept inside a sensing chamber to perform the sensing experiment at 27 °C. Changes in resistivity were assessed with different concentrations of gases. The response of the sensor was obtained using the following equation:

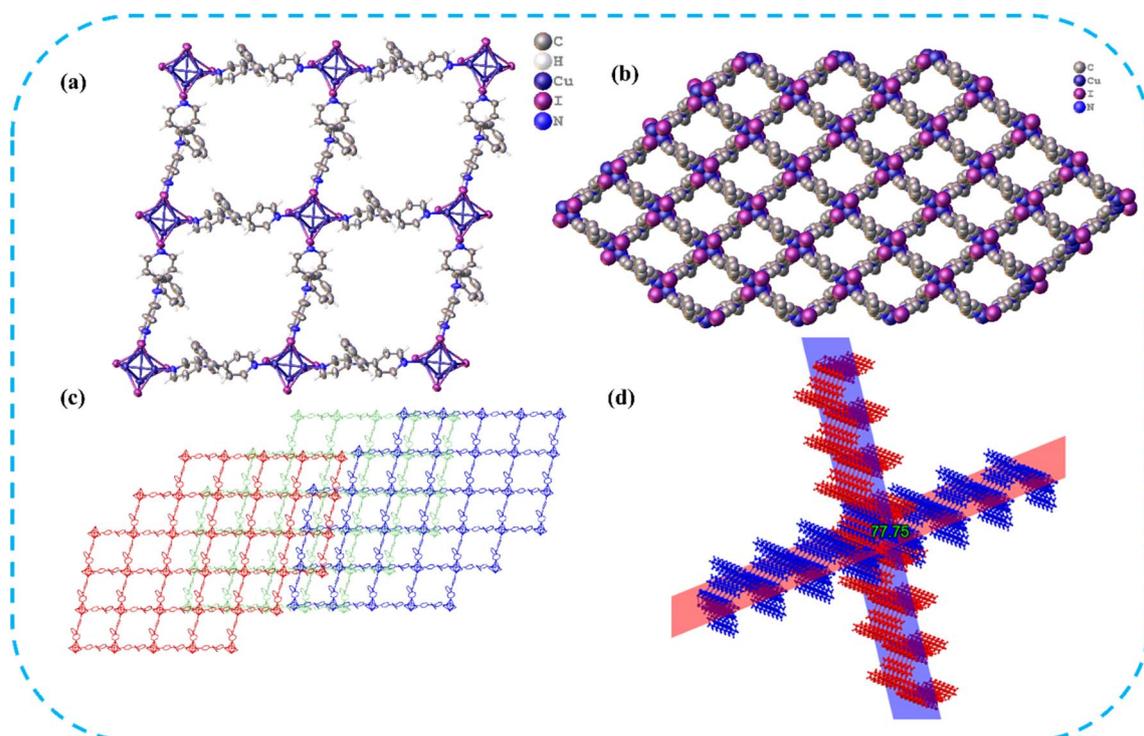$$R = \left(\frac{R_a - R_g}{R_g} \right) \times 100 \tag{1}$$

Fig. 1 (a) 2D sheet of the rhombus grid network of **Cu-MOF** (b) Space filled model of 2D **Cu-MOF**. (c) C−H···I interactions leading to parallel stacking of sheets. (d) Interpenetration of two sheets.
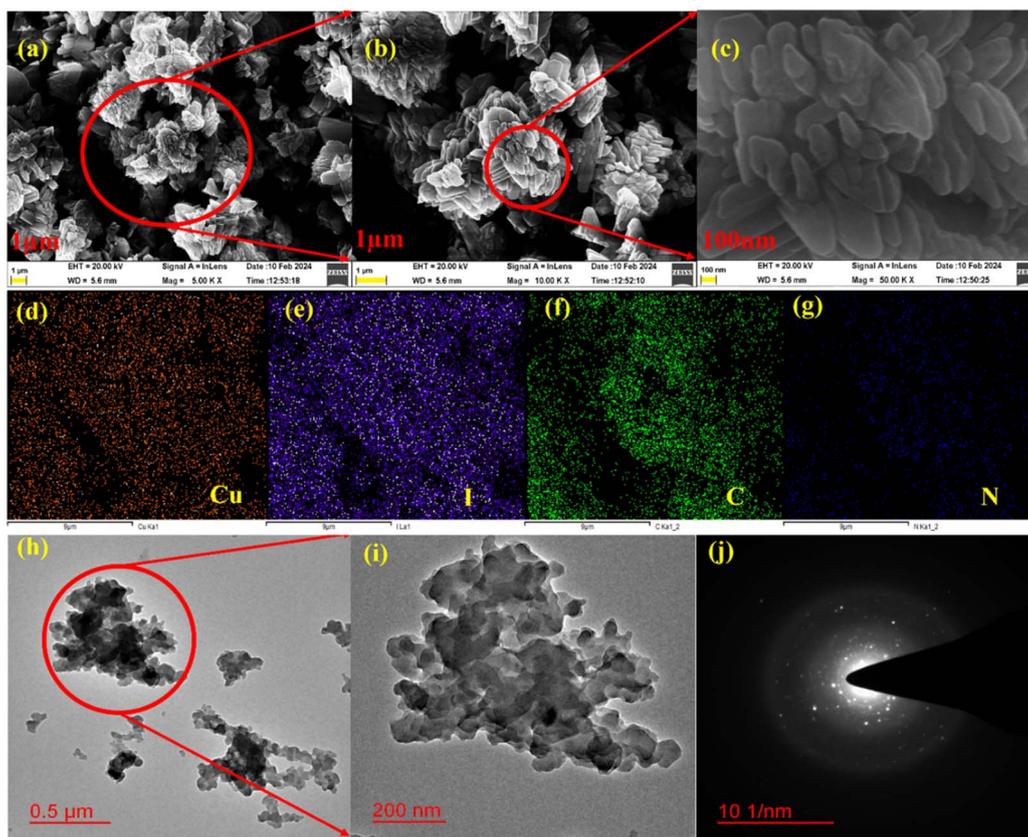
11418 | *J. Mater. Chem. A*, 2025, **13**, 11416–11424

This journal is © The Royal Society of Chemistry 2025

Fig. 2 (a–c) FE-SEM images of **Cu-MOF**. (d–e) Elemental mapping of elements present in **Cu-MOF**. (h and i) TEM images of **Cu-MOF**. (j) SAED patterns from TEM (g and h).

Here, R_a and R_g are the resistance of the sensing device in ambient air and during gas exposure, respectively. Moreover, the response (τ_{res}) and recovery time (τ_{rec}) of the fabricated **Cu-MOF** sensor are defined as the 0 to 90% change in resistance and 100 to 10% change during test gas adsorption and desorption, respectively.

Initially, the responses of the **Cu-MOF** sensor toward different reducing and oxidizing gases were investigated (Fig. 3a). The **Cu-MOF** sensor shows response values of −80%, 630%, −48%, 220%, 110%, 60%, −64% and −49% to interfering gases such as H_2S (100 ppm), NO_2 (100 ppm), MeOH (100 ppm), SO_2 (100 ppm), CO_2 (200 ppm), CH_4 (500 ppm), NH_3 (100 ppm) and CO (200 ppm), respectively. The selectivity factors of the **Cu-MOF** sensor for 100 ppm of NO_2 are calculated to be $SNO_2/SH_2S = 7.8$, $SNO_2/SMeOH = 13.1$, $SNO_2/SSO_2 = 2.9$, $SNO_2/SCO_2 = 5.7$, $SNO_2/SCH_4 = 10.5$, $SNO_2/SNH_3 = 9.49$ and $SNO_2/SCO = 12.8$ representing a significantly high selectivity toward NO_2 compared to other oxidizing and reducing gases. Afterward, the dynamic sensing performance of the **Cu-MOF** sensor at different concentrations of NO_2 was investigated at 27 °C (Fig. 3b). As the concentration of NO_2 decreases from 100 ppm to 100 ppb, the response value of **Cu-MOF** sensors also decreases from 630 to 98%. Most importantly, the **Cu-MOF** sensor exhibited a quick response/recovery time of only 11.6/13 seconds and 9.1/10.8 seconds at 10 ppm and 100 ppm NO_2

concentrations, respectively (Fig. 3c). These transient times are one of the quickest among the reported MOF-based NO_2 sensors (Fig. 4a and Table S2†).

Furthermore, the LOD and LOQ values of the **Cu-MOF** sensor were found to be 3.5 and 11.7 ppb, respectively, highlighting its excellent sensitivity (Fig. 3d). The repeatability of the sensor was also studied up to 11 cycles, and complete consistency was observed with no significant drop in performance (Fig. 3e). To evaluate the reproducibility and selectivity of the sensor towards NO_2 under varying relative humidity (RH) conditions, we measured the response of four different devices A, B, C, and D, prepared similarly. The response was recorded at room temperature with RH levels of 36%, 51%, 71%, 84%, and 98.3% (Fig. 3f). All four devices showed minimal variation in response, with only a small deviation in performance. However, as RH increased from 36% to 98%, the response of the **Cu-MOF** sensor gradually decreased from 630% to 151%. Despite this, the sensor maintained a significant response, demonstrating its robustness. The decline in response can be attributed to the reduced availability of active sites for analyte interaction. Furthermore, long-term stability of the devices was assessed, which showed minor changes in response during 60 days of analysis (Fig. S13†).

To understand the sensing mechanism, we first recorded the *ex situ* PXRD and ATR-IR spectra of the **Cu-MOF** sensor after
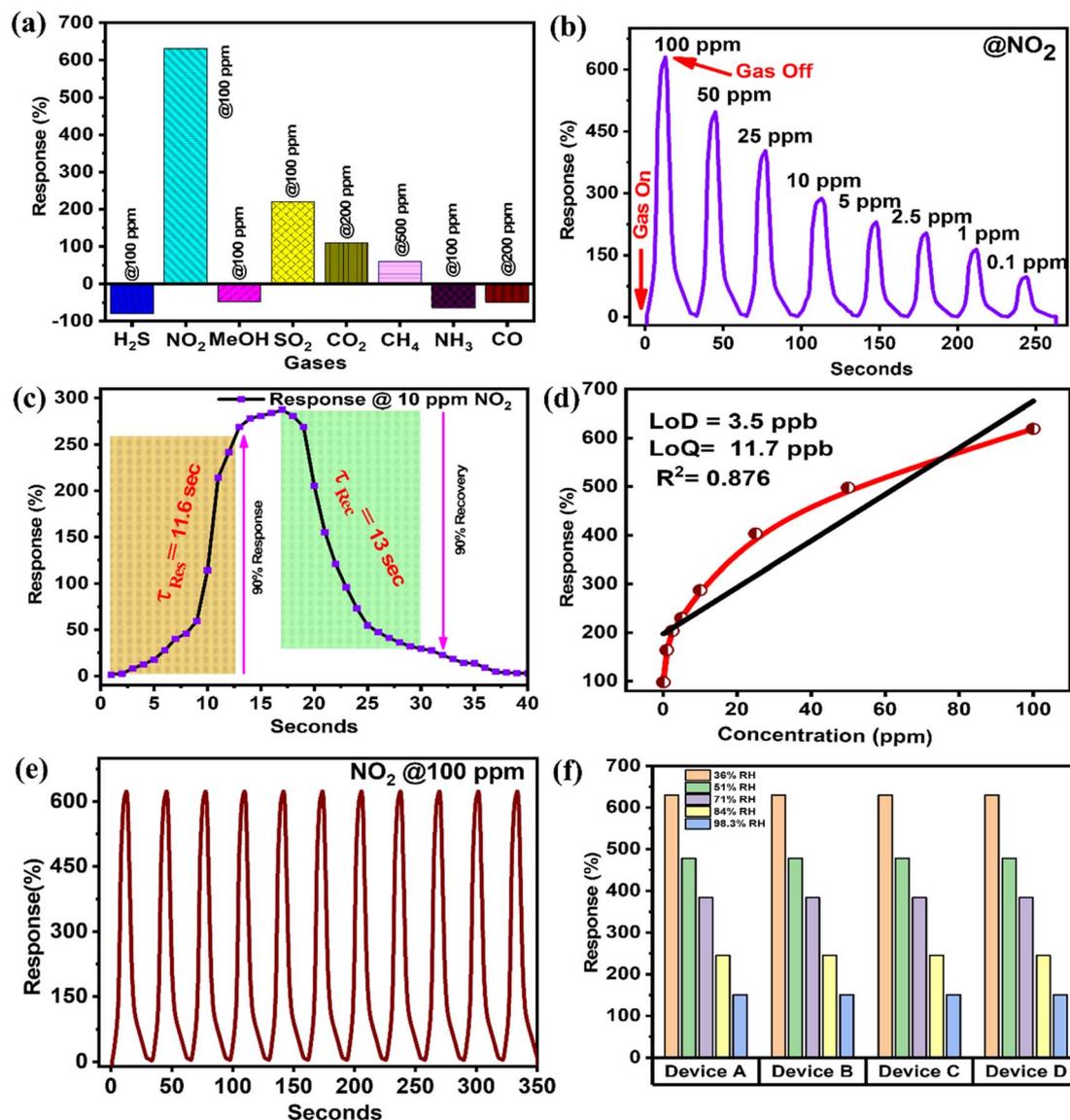
Fig. 3 (a) Sensor selectivity analysis for the **Cu-MOF** sensor with interfering gases, (b) **Cu-MOF** sensor response for various NO_2 concentrations at room temperature, (c) transient profile of the **Cu-MOF**, (d) LOD and LOQ of **Cu-MOF**, (e) repeatability of the **Cu-MOF** sensor performance for eleven consecutive cycles and (f) changes in response with increasing humidity and reproducibility.

exposure to NO_2 gas over the powder sample. After exposure to NO_2, ATR-IR analysis revealed a new peak at 1643 cm^{-1}, which corresponds to molecularly adsorbed NO_2.[47,48] Additionally, a slight shift in the rest of the spectra confirms the interaction between the analyte and the sensing material (Fig. 4b). The sharp PXRD patterns established the structural integrity of the **Cu-MOF** even after NO_2 exposure (Fig. S14†). The presence of robust Cu_4I_4 SBUs does not allow any structural disintegration during gas interaction, which is probably also responsible for excellent reversibility during sensing experiments. XPS analysis was conducted before and after gas exposure for deeper insight into the changes in surface chemistry, oxidation states, and material–analyte interaction (Fig. S15†). Peaks at 952.08 eV and 932.08 eV indicate the presence of Cu(ɪ) (Cu2p) and 618.88 eV and 630.28 eV correspond to iodine (I3d), while peaks at

400.28 eV and 284.28 eV correspond to nitrogen (N1s) and carbon (C1s), respectively (Fig. S16†). After exposing the material to NO_2, two distinct peaks at 934 and 932 eV appear, suggesting the presence of both Cu^{2+} and Cu^+ (Fig. 4c andd).[13,38,49,50] Moreover, a new peak at 406.7 eV in the N1s spectrum can be designated to the presence of metal-coordinated NO_2 molecules (Fig. 4e and f).[13,19] Furthermore, UV-Vis DRS study suggests that exposing **Cu-MOF** to NO_2 gas led to a decrease in the band gap of the material (Fig. S17†). These observations establish that NO_2 accepts an electron from Cu(ɪ) and oxidizes it to Cu(ɪɪ) during the interaction, leading to a change in electrical response.

To elucidate the experimental findings, we conducted density functional theory (DFT) calculations to simulate the adsorption of NO_2 on a 2D model of **Cu-MOF**. DFT calculations

11420 | J. Mater. Chem. A, 2025, **13**, 11416–11424

This journal is © The Royal Society of Chemistry 2025
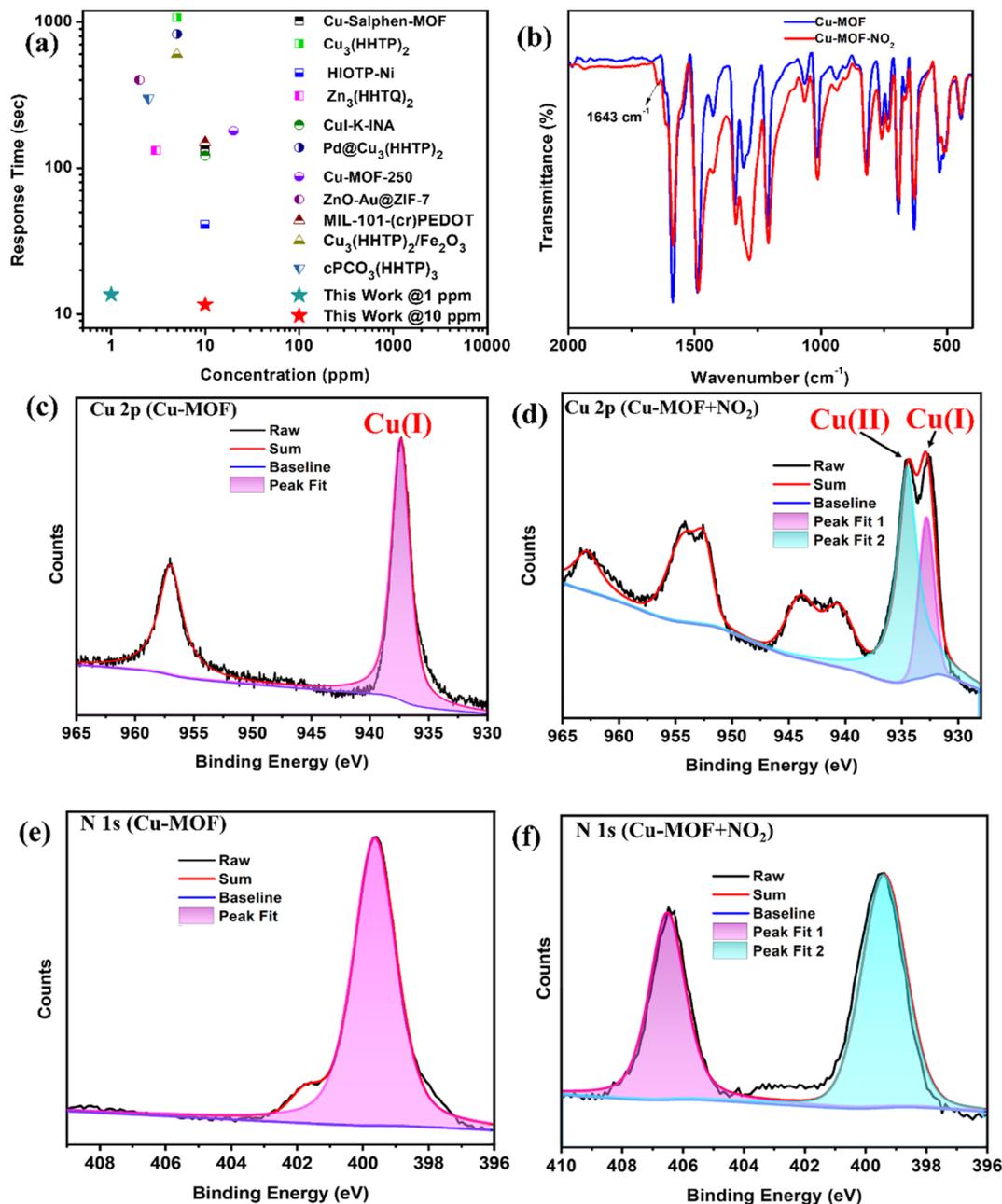
Fig. 4 (a) Response time comparison of the **Cu-MOF** sensor with the reported MOFs and hybrid MOF-based NO_2 sensors at room temperature (Tables S2 and S3†). (b) IR-spectra of the **Cu-MOF** sensor before and after NO_2 exposure. High-resolution Cu2p XPS spectra (c) before NO_2 exposure and (d) after NO_2 exposure; high-resolution N1s XPS spectra (e) before NO_2 exposure and (f) after NO_2 exposure.

were performed for structural optimization and electronic property analysis. Structural optimizations were performed using the Linear Combination of Atomic Orbitals (LCAO) basis set as implemented in the QuantumATK software.[51] All other calculations, such as adsorption energy, electronic properties, and charge density, were calculated using the plane wave basis Quantum Espresso code suite for enhanced accuracy.[52,53] The exchange–correlation interactions were addressed using the revised Perdew–Burke–Ernzerhof (RPBE) functional, which was designed to describe the adsorption process more accurately within the Generalized Gradient Approximation (GGA)

framework.[54,55] A $2 \times 2 \times 1$ k-point mesh was employed during the structural optimization process and all subsequent calculations utilized a denser $4 \times 4 \times 1$ k-point mesh in sampling the Brillouin zone. Long-range interactions were accounted for using the Grimme-D3 dispersion correction method.[56,57] Mulliken population analysis was calculated using the QuantumATK code suite which provided insights into the system's charge distribution.

The experimental findings from XPS suggested the adsorption of NO_2 molecules onto the Cu site. Based on this observation, the optimization was done with initial configurations

This journal is © The Royal Society of Chemistry 2025

J. Mater. Chem. A, 2025, **13**, 11416–11424 | **11421**

positioning the NO_2 molecule at a distance of 2.00 Å above the cubane tetramer (Cu_4I_4) cluster. This starting point was chosen to reflect the likely interaction between the analyte and the substrate. The post-optimization analysis elucidated that the NO_2 gas was effectively adsorbed onto the Cu atom of the Cu_4I_4. Furthermore, enhanced stability was observed when the N atom of the analyte interacts with the Cu atom compared to the O atom of the analyte. The distance between the adsorbed NO_2 molecules and the Cu atom was found to be 2.74 Å. Therefore, the DFT structural optimization studies further support experimental observation that the NO_2 analyte exhibits a preferential binding affinity towards the Cu sites of Cu_4I_4 within the **Cu-MOF**. The structures of bare and most stable NO_2 adsorbed 2D **Cu-MOF** (NO_2–**Cu-MOF**) are depicted in Fig. 5a and b.

The calculated adsorption energy of −0.286 eV for the most stable adsorbed configuration substantiates the energetic feasibility of the adsorption process. Additionally, theoretical calculations provided further predicts that NO_2 forms a coordinate chemical bond with the **Cu-MOF** at a distance of 2.05 Å from Cu_4I_4 cluster, whereas NH_3 and CO_2, for example, interact only *via* physical adsorption, with larger distances of 3.26 Å and 3.92 Å, respectively. Moreover, the calculated adsorption energies underscore the differences in interaction strength. For NH_3 and CO_2, the adsorption energies are −0.214 eV and −0.116 eV, respectively, which are notably weaker than the −0.286 eV adsorption energy for NO_2. This strong chemical interaction with NO_2 results in a more significant impact on the MOF's conductivity compared to other physically adsorbed gases (Fig.

S18†). To elucidate the charge transfer characteristics, we conducted a comprehensive Mulliken charge population analysis. Table S4† presents the calculated Mulliken charges of atoms within the Cu_4I_4 cubane tetramer and the adsorbate NO_2 molecule. The analysis reveals that the Cu atom directly interacts with the NO_2 gas with a subtle reduction in electron density, while NO_2 acquires a marginally increased electron population compared to its gas phase molecular form. This observation implies a minor charge transfer from the **Cu-MOF** to the NO_2 molecule upon adsorption. To further corroborate these findings, we plotted the charge density difference, comparing the electronic charge distribution before and after NO_2 adsorption, as illustrated in Fig. 5. In the plot, regions of charge accumulation are depicted in golden yellow (Fig. 5c), while areas of charge depletion are represented in light green (Fig. 5d). The plot unambiguously demonstrates electron transfer from the Cu atom to the NO_2 molecule, providing compelling evidence for the redistribution of charge occurring during the adsorption process.

We further investigated the electronic structure modifications induced by NO_2 adsorption by calculating the density of states for both the bare **Cu-MOF** and NO_2-**Cu-MOF**, as illustrated in Fig. S19.† Upon NO_2 adsorption, a notable shift in the Fermi level (E_F) towards the valence band states was observed. This downward shift of the E_F is characteristic of p-type doping in semiconductor materials. Consequently, the adsorption of NO_2 on the **Cu-MOF** appears to introduce hole carriers into the system. This observation along with experimental results
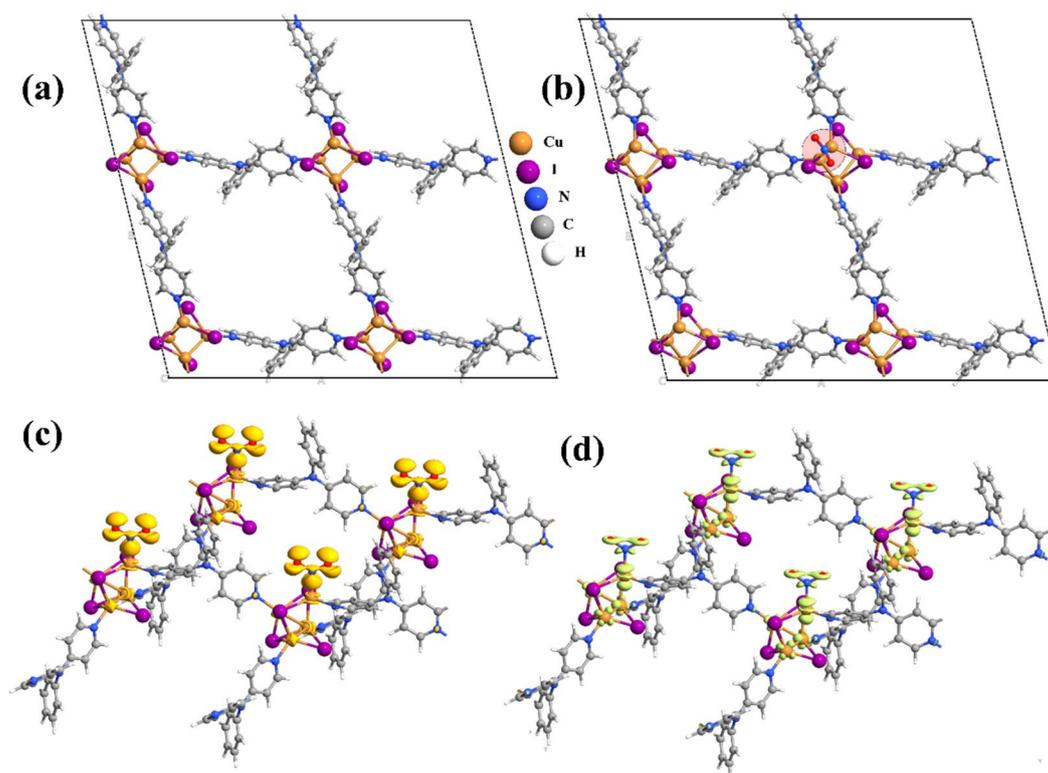

Fig. 5 The equilibrium structures of (a) bare **Cu-MOF** and (b) NO_2–**Cu-MOF**. The electronic charge density difference plot depicting (c) accumulation region (golden yellow) and (d) depletion region (light green).

11422 | *J. Mater. Chem. A*, 2025, **13**, 11416–11424

This journal is © The Royal Society of Chemistry 2025

suggests that the electrical response in the NO_2-**Cu-MOF** is predominantly governed by hole conductivity. Overall, the theoretical study provides valuable insights into the preferential binding mechanism of NO_2 on the **Cu-MOF** and the changes induced in its electronic properties, which corroborate the experimental results.

Conclusion

In this study, we have successfully demonstrated the potential of semiconducting Cu(I) MOF as a chemiresistive gas sensor for NO_2 detection. The **Cu-MOF**, constructed from Cu_4I_4 SBUs and the PDPA ligand, forms a 2D network that was thoroughly characterized by IR, SCXRD, PXRD, FE-SEM, TEM, and XPS. The mesoporous nature and semiconducting behavior of **Cu-MOF** offer distinct advantages for chemiresistive gas sensing. The sensor exhibited excellent performance in detecting NO_2 at room temperature, achieving a LOD of 3.5 ppb and exceptionally fast response and recovery times of less than 15 seconds. This performance surpasses that of many reported state-of-the-art NO_2 sensors, making the **Cu-MOF** a strong candidate for practical sensing applications. The sensing mechanism was further investigated through IR, PXRD, XPS, and DFT analyses, indicating electron transfer from the Cu(I) center to NO_2 during adsorption, resulting in a distinct and measurable change in electrical response. The straightforward synthesis and the outstanding performance of the **Cu-MOF**-based sensor in selective NO_2 detection highlight its potential for industrial and environmental gas monitoring.

Data availability

All the data will be made available on reviewers' request.

Conflicts of interest

The authors declare no competing interests.

Acknowledgements

References

1 L. S. Xie, G. Skorupskii and M. Dincă, *Chem. Rev.*, 2020, **120**, 8536–8580.

2 L. Sun, M. G. Campbell and M. Dincă, *Angew. Chem., Int. Ed.*, 2016, **55**, 3566–3579.

3 D. D. Medina, A. Mähringer and T. Bein, *Isr. J. Chem.*, 2018, **58**, 1089–1101.

4 M. Ko, L. Mendecki and K. A. Mirica, *Chem. Commun.*, 2018, **54**, 7873–7891.

5 H. Banda, J.-H. Dou, T. Chen, N. J. Libretto, M. Chaudhary, G. M. Bernard, J. T. Miller, V. K. Michaelis and M. Dincă, *J. Am. Chem. Soc.*, 2021, **143**, 2285–2292.

6 M. Wang, R. Dong and X. Feng, *Chem. Soc. Rev.*, 2021, **50**, 2764–2793.

7 Y. Lu, P. Samorì and X. Feng, *Acc. Chem. Res.*, 2024, **57**, 1985–1996.

8 W. Liu, G. Yuan, S. Jiang, Y. Shi and H. Pang, *Chem. Eur J.*, 2024, **30**, e202402747.

9 S. Mishra, M. K. Singh, D. Pandey, D. K. Rai and A. Raghuvanshi, *J. Mater. Chem. A*, 2024, **12**, 4534–4543.

10 C. Park, J. W. Baek, E. Shin and I.-D. Kim, *ACS Nanosci. Au*, 2023, **3**, 353–374.

11 X. Wang, Y. Chen, Z. Zeng, M. Yan, X. Jia, P. Hu, J. Xu, Z. Xue and J. Xu, *Mater. Sci. Eng. R Rep.*, 2024, **160**, 100819.

12 X. Yan, J. Chen, X. Su, J. Zhang, C. Wang, H. Zhang, Y. Liu, L. Wang, G. Xu and L. Chen, *Angew. Chem., Int. Ed.*, 2024, **63**, e202408189.

13 P. Chen, X. Su, C. Wang, G. Zhang, T. Zhang, G. Xu and L. Chen, *Angew. Chem., Int. Ed.*, 2023, **62**, e202306224.

14 Y. Jo, Y. K. Jo, J. Lee, H. W. Jang, I. Hwang and D. J. Yoo, *Adv. Mater.*, 2023, **35**, 2206842.

15 W.-T. Koo, J.-S. Jang and I.-D. Kim, *Chem*, 2019, **5**, 1938–1963.

16 A. Sharma, S. B. Eadi, H. Noothalapati, M. Otyepka, H.-D. Lee and K. Jayaramulu, *Chem. Soc. Rev.*, 2024, **53**, 2530–2577.

17 B. Mohan, Virender, R. K. Gupta, A. J. L. Pombeiro, A. A. Solovev and G. Singh, *Adv. Funct. Mater.*, 2024, **34**, 2405231.

18 M. G. Campbell, D. Sheberla, S. F. Liu, T. M. Swager and M. Dincă, *Angew. Chem., Int. Ed.*, 2015, **54**, 4349–4352.

19 Z.-F. Wu, C. Wang, X. Liu, K. Tan, Z. Fu, S. J. Teat, Z.-W. Li, X. Hei, X.-Y. Huang, G. Xu and J. Li, *J. Am. Chem. Soc.*, 2023, **145**, 19293–19302.

20 M. G. Campbell, S. F. Liu, T. M. Swager and M. Dincă, *J. Am. Chem. Soc.*, 2015, **137**, 13780–13783.

21 Z. Meng, R. M. Stolz and K. A. Mirica, *J. Am. Chem. Soc.*, 2019, **141**, 11929–11937.

22 D. Pandey, C. Patel, S. Mishra, S. Mukherjee and A. Raghuvanshi, *ACS Appl. Nano Mater.*, 2024, **7**, 15833–15840.

23 S. Mishra, C. Patel, D. Pandey, S. Mukherjee and A. Raghuvanshi, *Small*, 2024, **20**, 2311448.

24 Z. Ma, Y. Zhang, Z. Xue, Y. Fan, L. Wang, H. Wang, A. Zhong and J. Xu, *ACS Sens.*, 2024, **9**, 1906–1915.

25 D. Pandey, A. Mishra, L. S. Kharabe, S. K. Maurya and A. Raghuvanshi, *Cryst. Growth Des.*, 2024, **24**, 6051–6059.

26 D. Pandey, M. K. Singh, S. Mishra, D. K. Rai and A. Raghuvanshi, *J. Mater. Chem. A*, 2024, **12**, 27355–27363.

27 E. Cariati, E. Lucenti, C. Botta, U. Giovanella, D. Marinotto and S. Righetto, *Coord. Chem. Rev.*, 2016, **306**, 566–614.

28 J. Troyano, F. Zamora and S. Delgado, *Chem. Soc. Rev.*, 2021, **50**, 4606–4628.

29 A. Raghuvanshi, C. Strohmann, J. Tissot, S. Clément, A. Mehdi, S. Richeter, L. Viau and M. Knorr, *Chem. Eur J.*, 2017, **23**, 16479–16483.

30 H. E. Stokinger, *J. Air Pollut. Control Assoc.*, 1958, **8**, 129–137.

31 J. Zhang, X. Liu, G. Neri and N. Pinna, *Adv. Mater.*, 2016, **28**, 795–831.

32 T. L. Guidotti, *Environ. Res.*, 1978, **15**, 443–472.

33 C. Ren and S. Tong, *Environ. Health*, 2008, **7**, 56.

34 Q. Li, W. Zeng and Y. Li, *Sens. Actuators, B*, 2022, **359**, 131579.

35 H. Kosaka, M. Uozumi and I. Tyuma, *Free Radic. Biol. Med.*, 1989, **7**, 653–658.

36 A. J. Timmons and M. D. Symes, *Chem. Soc. Rev.*, 2015, **44**, 6708–6722.

37 A. M. Wright, C. Sun and M. Dincă, *J. Am. Chem. Soc.*, 2021, **143**, 681–686.

38 H. Roh, D. Kim, Y. Cho, Y. Jo, J. A. Del Alamo, H. J. Kulik, M. Dincă and A. Gumyusenge, *Adv. Mater.*, 2024, **36**, 2312382.

39 W. Koo, S. Kim, J. Jang, D. Kim and I. Kim, *Adv. Sci.*, 2019, **6**, 1900250.

40 X. Su, Z. Zhong, X. Yan, T. Zhang, C. Wang, Y.-X. Wang, G. Xu and L. Chen, *Angew. Chem., Int. Ed.*, 2023, **62**, e202302645.

41 S.-Q. Bai, K. L. Ke, D. J. Young and T. S. A. Hor, *J. Organomet. Chem.*, 2017, **849–850**, 137–141.

42 S.-S. Zhao, L. Wang, Y. Liu, L. Chen and Z. Xie, *Inorg. Chem.*, 2017, **56**, 13975–13981.

43 P. K. Pal, A. Mukherjee, A. Ghosh and G. K. Patra, *J. Mol. Struct.*, 2014, **1059**, 332–337.

44 D. Sun, S. Yuan, H. Wang, H.-F. Lu, S.-Y. Feng and D.-F. Sun, *Chem. Commun.*, 2013, **49**, 6152.

45 S. Khatua, S. Goswami, S. Biswas, K. Tomar, H. S. Jena and S. Konar, *Chem. Mater.*, 2015, **27**, 5349–5360.

46 H.-C. Fan, X. Xia, Y.-B. Zeng, Q.-F. Wang, D. Chen, S.-C. Qin, C.-Q. Wang, Q.-E. Cao and L.-Y. Zheng, *Small Struct.*, 2022, **3**, 2200030.

47 M. Schulz, A. Gehl, J. Schlenkrich, H. A. Schulze, S. Zimmermann and A. Schaate, *Angew. Chem., Int. Ed.*, 2018, **57**, 12961–12965.

48 K. Nakamoto, in *Handbook of Vibrational Spectroscopy*, ed. J. M. Chalmers and P. R. Griffiths, Wiley, 1st edn, 2001.

49 C. Park, W. Koo, S. Chong, H. Shin, Y. H. Kim, H. Cho, J. Jang, D. Kim, J. Lee, S. Park, J. Ko, J. Kim and I. Kim, *Adv. Mater.*, 2021, **33**, 2101216.

50 H. Lim, H. Kwon, H. Kang, J. E. Jang and H.-J. Kwon, *Nat. Commun.*, 2023, **14**, 3114.

51 S. Smidstrup, T. Markussen, P. Vancraeyveld, J. Wellendorff, J. Schneider, T. Gunst, B. Verstichel, D. Stradi, P. A. Khomyakov, U. G. Vej-Hansen, M.-E. Lee, S. T. Chill, F. Rasmussen, G. Penazzi, F. Corsetti, A. Ojanperä, K. Jensen, M. L. N. Palsgaard, U. Martinez, A. Blom, M. Brandbyge and K. Stokbro, *J. Phys. Condens. Matter*, 2020, **32**, 015901.

52 P. Giannozzi, S. Baroni, N. Bonini, M. Calandra, R. Car, C. Cavazzoni, D. Ceresoli, G. L. Chiarotti, M. Cococcioni, I. Dabo, A. Dal Corso, S. De Gironcoli, S. Fabris, G. Fratesi, R. Gebauer, U. Gerstmann, C. Gougoussis, A. Kokalj, M. Lazzeri, L. Martin-Samos, N. Marzari, F. Mauri, R. Mazzarello, S. Paolini, A. Pasquarello, L. Paulatto, C. Sbraccia, S. Scandolo, G. Sclauzero, A. P. Seitsonen, A. Smogunov, P. Umari and R. M. Wentzcovitch, *J. Phys. Condens. Matter*, 2009, **21**, 395502.

53 P. Giannozzi, O. Andreussi, T. Brumme, O. Bunau, M. Buongiorno Nardelli, M. Calandra, R. Car, C. Cavazzoni, D. Ceresoli, M. Cococcioni, N. Colonna, I. Carnimeo, A. Dal Corso, S. De Gironcoli, P. Delugas, R. A. DiStasio, A. Ferretti, A. Floris, G. Fratesi, G. Fugallo, R. Gebauer, U. Gerstmann, F. Giustino, T. Gorni, J. Jia, M. Kawamura, H.-Y. Ko, A. Kokalj, E. Küçükbenli, M. Lazzeri, M. Marsili, N. Marzari, F. Mauri, N. L. Nguyen, H.-V. Nguyen, A. Otero-de-la-Roza, L. Paulatto, S. Poncé, D. Rocca, R. Sabatini, B. Santra, M. Schlipf, A. P. Seitsonen, A. Smogunov, I. Timrov, T. Thonhauser, P. Umari, N. Vast, X. Wu and S. Baroni, *J. Phys. Condens. Matter*, 2017, **29**, 465901.

54 B. Hammer, L. B. Hansen and J. K. Nørskov, *Phys. Rev. B*, 1999, **59**, 7413–7421.

55 J. P. Perdew, K. Burke and M. Ernzerhof, *Phys. Rev. Lett.*, 1996, **77**, 3865–3868.

56 S. Grimme, J. Antony, S. Ehrlich and H. Krieg, *J. Chem. Phys.*, 2010, **132**, 154104.

57 S. Grimme, S. Ehrlich and L. Goerigk, *J. Comput. Chem.*, 2011, **32**, 1456–1465.

11424 | *J. Mater. Chem. A*, 2025, **13**, 11416–11424

This journal is © The Royal Society of Chemistry 2025